

# Optimal design of experiment

Oliwer Sliczniuk<sup>a,\*</sup>, Pekka Oinas<sup>a</sup>

<sup>a</sup>Aalto University, School of Chemical Engineering, Espoo, 02150, Finland

## ARTICLE INFO

### Keywords:

Supercritical extraction  
Optimal design of experiment  
Mathematical modelling

## ABSTRACT

This study investigates the process of chamomile oil extraction from flowers. A parameter-distributed model consisting of a set of partial differential equations is used to describe the governing mass transfer phenomena in a cylindrical packed bed with solid chamomile particles under supercritical conditions using carbon dioxide as a solvent. The concept of quasi-one-dimensional flow is applied to reduce the number of spatial dimensions. The flow is assumed to be uniform across any cross-section, although the area available for the fluid phase can vary along the extractor. The physical properties of the solvent are estimated from the Peng-Robinson equation of state. The empirical correlations used in the model are based on the set of laboratory experiments performed under multiple constant operating conditions: 30 – 40 °C, 100 – 200 bar, and  $3.33 - 6.67 \cdot 10^{-5}$  kg/s. A model-based design of experiments with D-optimality criterion is applied to improve the precision of the correlation parameters by designing a new dynamic experiment. The mass flow rate and inlet temperature are used as decision variables to maximize the Fisher Information embedded in the yield curve with respect to the empirical correlations.

## 1. Introduction

Supercritical CO<sub>2</sub> is defined as carbon dioxide that is pressurized and heated above its critical point (31.1 °C, 74 bar). Depending on the operating conditions, the fluid properties such as viscosity and density can vary, which leads to multiple industrial applications of CO<sub>2</sub>.

One of the most popular applications of supercritical CO<sub>2</sub> is the extraction of essential oils, as described by many researchers, for example, by Sodeifian and Sajadian [1], Reverchon et al. [2] or Sovova [3]. Traditional methods, such as distillation and organic solvent extraction, are commonly employed but have drawbacks. Distillation involves high temperatures that can lead to the thermal degradation of heat-sensitive compounds. This limitation has increased the popularity of alternative techniques, such as supercritical fluid extraction. Supercritical CO<sub>2</sub> is appealing due to its distinctive properties: it is inflammable, non-toxic and non-corrosive. Supercritical fluids can exhibit both gas- and liquid-like properties, allowing for adjustable dissolving power through changes in operating conditions.

The applications of supercritical carbon dioxide are not limited only to an extraction process but can also be used for impregnation, as described by Weidner [4] or Machado et al. [5]. Impregnation is defined as modifying the properties of bulk substances by physically or chemically binding/adsorbing impregnates to a bulk material or surface, such as the hydrophobization of surfaces. The main advantage of using supercritical CO<sub>2</sub> is that, after depressurization, it desorbs from the surface and evaporates, leaving a solvent-free product. On the other hand, the main disadvantage of using carbon dioxide for impregnation is the low solubility of many drugs of interest. The study of Ameri et al. [6] investigates the loading of lansoprazole into polymers

using supercritical carbon dioxide and examines how various parameters, such as temperature, pressure, and time, affect the drug loading efficiency. The results indicate that increasing any of these parameters enhances drug loading, with temperature having the most significant impact. Fathi et al. [7] explored the use of supercritical carbon dioxide to enhance the bioavailability of ketoconazole by impregnating it into water-soluble polymers, specifically polyvinylpyrrolidone and hydroxypropyl methylcellulose. Utilizing a Box-Behnken design, the researchers optimized the impregnation process by varying pressure, temperature, and time, achieving increase in drug loadings ranging.

Another application of supercritical CO<sub>2</sub> is nanoparticle formation, as investigated by Padrela et al. [8], Franco and De Marco [9] or Sodeifian et al. [10]. Supercritical carbon-dioxide-assisted technologies enable the production of different morphologies of different sizes, including nanoparticles and nanocrystals, by modulating the operating conditions. Supercritical fluid-based processes have advantages over techniques conventionally employed to produce nanosized particles or crystals, such as reduced use of toxic solvents. Moreover, the CO<sub>2</sub> is removed from the final product by simple depressurization. Sodeifian and Sajadian [11] investigated the solubility of Letrozole, a poorly water-soluble anticancer drug, in supercritical carbon dioxide with and without menthol as a solid co-solvent. The addition of menthol increased Letrozole's solubility by 7.1 times compared to supercritical CO<sub>2</sub> alone. Using the rapid expansion of supercritical solutions with solid co-solvent method, the average particle size of Letrozole was reduced to the nanoscale. Temperature was found to have the most significant impact on nanoparticle size reduction, while pressure had the least effect. The study of S. Ardestani et al. [12] explored the preparation of phthalocyanine green nano pigment using supercritical carbon dioxide as an antisolvent. The researchers employed the gas antisolvent technique to achieve nano-sized particles of the pigment. Sodeifian

\*Corresponding author

✉ oliwer.sliczniuk@aalto.fi (O. Sliczniuk)

ORCID(s): 0000-0003-2593-5956 (O. Sliczniuk); 0000-0002-0183-5558 (P. Oinas)

and Sajadian [13] analysed the production of amiodarone hydrochloride nanoparticles using an ultrasonic-assisted rapid expansion of supercritical solution into a liquid solvent method. By optimizing parameters such as pressure, temperature, and polymeric stabilizer concentration, the researchers achieved significant particle size reduction. Characterization techniques confirmed the successful formation of nanoparticles with improved properties.

This study investigates the extraction of essential oil from chamomile flowers (*Matricaria chamomilla* L.) via supercritical fluid extraction techniques and the modelling of this process. Chamomile is a medicinal herb widely cultivated in southern and eastern Europe — in countries such as Germany, Hungary, France and Russia. It can also be found outside Europe, for instance in Brazil, as discussed by Singh et al. [14]. This plant is distinguished by its hollow, bright gold cones, housing disc or tubular florets and surrounded by about fifteen white ray or ligulate florets. Chamomile has been used for its medicinal benefits, serving as an anti-inflammatory, antioxidant, mild astringent, and healing remedy. Extracts of chamomile are widely used to calm nerves and mitigate anxiety, hysteria, nightmares, insomnia and other sleep-related conditions, according to Srivastava [15]. Orav et al. [16] reported that oil yields from dried chamomile samples ranged from 0.7 to 6.7 mL/kg. The highest yields of essential oil, between 6.1 and 6.7 mL/kg, were derived from chamomile sourced from Latvia and Ukraine. In comparison, chamomile from Armenia exhibited a lower oil content of 0.7 mL/kg. Milovanovic and Grzegorzczak [17] extracted oils from Roman chamomile seeds in a two-stage process. First supercritical carbon dioxide at pressures up to 450 bar and temperatures up to 60 °C was used for the first extraction. Then, the authors re-extracted using supercritical CO<sub>2</sub> with the addition of ethanol. By optimization in operating pressure, temperature, production cost, fraction of milled seeds, and co-solvent addition, the amount of separated chamomile oil increased from 2.4 to 18.6% and the content of unsaturated fatty acids up to 88.7%.

The literature offers various mathematical models to describe the extraction of valuable compounds from biomass. Selecting a process model is case-dependent and requires analysis of each model's specific assumptions about mass transfer and thermodynamic equilibrium.

Depending on the needs one of two approaches can be considered while developing a mathematical model for the extraction process. A model, which is based on a multiple regression can be used if the relation between inputs and outputs is the only of interests. Sodeifian et al. [18] investigated an influence of pressure, temperature and particle size on the extraction efficiency of oil from *dracocephalum kotschy boiss* seed. The second order polynomial model was applied to obtain the corresponding response surface and to identify the optimum operating conditions. The study of Sodeifian et al. [19] investigates the of essential oil from *Eryngium billardieri*, focusing on optimizing extraction conditions and developing a mathematical model based on the second order polynomial to predict the process yield. The researchers

employed a simulated annealing algorithm to optimize parameters such as pressure, temperature, and extraction time, aiming to maximize oil efficiency.

Alternatively, a first principle model can be derived and applied to cover not only the input-output relations, but the phenomena occurring in the system. This approach allows for more detailed representation the system behaviour, but requires deeper understanding of the underlying physics and more rigorous experiments.

Goto et al. [20] presented the shrinking core (SC) model, which describes a process of irreversible desorption that is followed by diffusion through the pores of a porous solid. When the mass transfer rate of the solute in the non-extracted inner region is significantly slower than in the outer region, where most of the solute has already been extracted or when the solute concentration exceeds its solubility in the solvent, a distinct boundary may form between the inner and outer regions. As extraction progresses, the core of the inner region shrinks. The model envisions supercritical CO<sub>2</sub> extraction as a sharp, inward-moving front, with a completely non-extracted core ahead of the front and a fully extracted shell behind it.

Sovova [3] proposed the broken-and-intact cell (BIC) model, which assumes that a portion of the solute, initially stored within plant structures and protected by cell walls, is released during the mechanical breakdown of the material. The solute located in the region of broken cells near the particle surface is directly exposed to the solvent, while the core of the particle contains intact cells with undamaged walls. This model describes three extraction phases: a fast extraction phase for accessible oil, a transient phase, and a slow phase controlled by diffusion. The model has been successfully applied to the extraction of grape oil (Sovová et al. [21]) and caraway oil (Sovova et al. [22]).

The supercritical fluid extraction (SFE) process can be treated similarly to heat transfer, considering solid particles as hot balls cooling down in a uniform environment. Bartle et al. [23] introduced the hot ball diffusion (HBD) model, where spherical particles with a uniformly distributed solute diffuse similarly to heat diffusion. Unlike the BIC model, where the solute is readily available on the particle surface, the HBD model is suited for systems with small quantities of extractable materials and is not limited by solubility. The model is particularly relevant when internal diffusion controls mass transfer, allowing results from single particles to be extended to the entire bed under uniform conditions. Reverchon et al. [2] have further elaborated on the HBD model and used it to simulate extraction processes.

Reverchon [24] proposed a model for extraction of essential oils, which are mainly located inside the vegetable cells in organules called vacuoles. Only a small fraction of essential oil might be near the particle surface due to the breaking up of cells during grinding or in epidermal hairs located on the leaf surface. The fraction of oil freely available on the particle surface should not be significant in the case of SFE from leaves. Consequently, SFE of essential oil from leaves should be mainly controlled by internal mass-transfer

resistance. Therefore, the external mass-transfer coefficient was neglected in the development of the model of Reverchon [24]. The mass balances were developed with the additional hypotheses that axial dispersion can be neglected and that the solvent density and flow rate are constant along the bed.

This work builds upon the linear kinetic model suggested by Reverchon [24], deriving fundamental governing equations to develop a comprehensive model for the chamomile oil extraction process. This model aims at control-oriented simplicity, assuming semi-continuous operation within a cylindrical vessel. The process involves a supercritical solvent being pumped through a fixed bed of finely chopped biomass to extract the solute, followed by separation of the solvent and solute in a flush drum to collect the extract. Parameters such as pressure ( $P$ ), feed flow rate ( $F$ ) and inlet temperature ( $T_{in}$ ) are adjustable and measurable, while the outlet temperature ( $T_{out}$ ) and the amount of product at the outlet can only be monitored. Figure 1 presents a simplified process flow diagram.

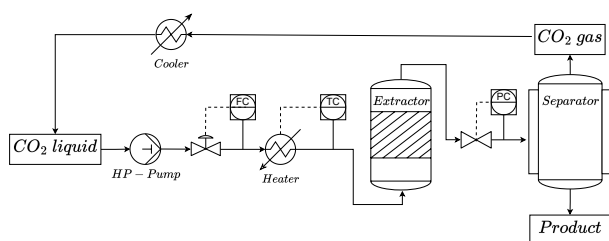


Figure 1: Process flow diagram.

Design of Experiments (DoE) is a structured approach that examines how various elements influence a particular result. By evaluating multiple factors at once, DoE allows the uncovering of the impacts of each element and their combinations, yielding a comprehensive comprehension of the entire system. DoE begins with determining an experiment's objectives and selecting the study's process factors. DoE aims to obtain the maximum information from an experimental apparatus modelled by devising experiments that will yield the most informative data in a statistical sense for use in parameter estimation and model validation.

The first ideas of DoE were introduced by Fisher [25], who described the fundamental problem of experimental design as deciding what pattern of factors combination will best reveal the properties of the response, and this response is influenced by the factors. This type of DoE views an experiment as simply connecting inputs with outputs and is therefore called a "black-box experiment design". It aims to select the combinations of factor values that will provide the most information on the input-output relationship in the presence of variation. This type's main class of statistical design techniques is the so-called factorial method. These methods are created to measure the additive effects on a response for each input factor and investigate the effects of interactions between factors. Factorial methods are unsuitable for situations where constraints exist on the output or internal states. They must also be better suited for dynamic

experiments, where inputs and outputs are complex time profiles. However, this group of methods is still widely used due to its simplicity.

Ramandi et al. [26] conducted a study to identify the variables with the greatest influence on the extraction yield of fatty acids from *Borago officinalis* L. flowers using Supercritical Fluid Extraction (SFE). A Full Factorial Design was employed as a screening method, resulting in a design matrix of 32 runs ( $2^5$ ) carried out randomly to minimize the impact of external factors. The low and high values for the factors were selected based on previous research. After determining the most significant variables, a Central Composite Design was applied to three factors—temperature, pressure, and volume of methanol co-solvent to optimize the SFE conditions. This allowed for the modeling of the response surface by fitting a second-order polynomial.

Similarly, Caldera et al. [27] conducted a study to optimize SFE variables, specifically extraction pressure, extraction temperature, and static extraction time, for the maximum extraction of carnosol and carnosic acid from Venezuelan rosemary (*Rosmarinus officinalis* L.) leaves. A  $2^3$  Full Factorial Design was initially used to examine these three variables. Based on the statistically significant variables, a Box-Behnken design was employed to create a matrix of 15 experiments, which was used to further optimize the SFE process for maximum carnosol and carnosic acid extraction using Response Surface Methodology.

As opposed to the "black-box" statistical experiment design methods, another form of optimal design has been developed, which takes explicit advantage of some knowledge of the structure underlying the system, represented by a mathematical model, in particular in the form of differential and algebraic equations. What characterises the model-based experiment design approach is :

1. the explicit use of the model equations and current parameters to predict the "information content" of the next experiment
2. the application of an optimisation framework to the solution of the resulting numerical problem

After an initial dataset has been collected and fitted to a mathematical model, the model undergoes further analysis. Additional experiments may be needed to differentiate between competing models that passed the preliminary tests. Once inadequate models are rejected, the remaining model may undergo another round of experiment design to enhance the precision of its parameters. This paper focuses on the final step of the validation procedure, known as model-based Design of Experiments (m-DoE), aimed at improving parameter precision. To the authors' knowledge, the m-DoE has not been applied to any case of supercritical extraction, so the further literature review provides examples of application in crystallization and pharmacology processes.

Chung et al. [28] applied model-based experimental design to a batch crystallization process with a cooling jacket. A dynamic programming formulation minimizes the

volume of a confidence hyper-ellipsoid for the estimated nucleation and growth parameters over the supersaturation profile and the seed characteristics, namely, the crystal mass, mean size, and width of the seed distribution. As a result, the accuracy of the parameter estimates can be improved by identifying the optimal temperature profile.

Duarte et al. [29] investigated compartment models incorporating Michaelis-Menten elimination kinetics for pharmacological applications. The authors designed both static and dynamic experiments for 2- and 3-compartment models using D-optimality criteria. The dynamic experiments for both models involved determining the initial concentration in the first compartment and optimizing the profile of the mass flow rate of the drug entering this compartment.

## 2. Materials and methods

### 2.1. Governing equations

Following the work of Anderson [30], the governing equations for a quasi-one-dimensional flow were derived. A quasi-one-dimensional flow refers to a fluid flow scenario assuming that the flow properties are uniformly distributed across any cross-section. This simplification is typically applied when the flow channel's cross-sectional area changes, such as through irregular shapes or partial filling of an extractor. According to this assumption, velocity and other flow properties change solely in the flow direction.

As discussed by Anderson [31], all flows are compressible, but some of them can be treated as incompressible since the velocities are low. This assumption leads to the incompressible condition:  $\nabla \cdot u = 0$ , which is valid for constant density (strict incompressible) or varying density flow. The assumption allows for removing acoustic waves and large perturbations in density and/or temperature. In the 1-D case, the incompressibility condition becomes  $\frac{du}{dz} = 0$ , so the fluid velocity is constant along the  $z$ -direction.

The set of quasi-one-dimensional governing equations in Cartesian coordinates is described by Equations 1 - 3:

$$\frac{\partial(\rho_f A_f)}{\partial t} + \frac{\partial(\rho_f A_f v)}{\partial z} = 0 \quad (1)$$

$$\frac{\partial(\rho_f v A_f)}{\partial t} + \frac{\partial(\rho_f A_f v^2)}{\partial z} = -A_f \frac{\partial P}{\partial z} \quad (2)$$

$$\frac{\partial(\rho_f e A_f)}{\partial t} + \frac{\partial(\rho_f A_f v e)}{\partial z} = -P \frac{\partial(A_f v)}{\partial z} + \frac{\partial}{\partial z} \left( k \frac{\partial T}{\partial z} \right) \quad (3)$$

where  $\rho_f$  is the density of the fluid,  $A_f$  is the function which describes a change in the cross-section,  $v$  is the velocity,  $P$  is the total pressure,  $e$  is the internal energy of the fluid,  $t$  is time and  $z$  is the spatial direction.

### 2.2. Extraction model

#### 2.2.1. Continuity equation

The previously derived quasi-one-dimensional continuity equation (Equation 1) is redefined by incorporating the function  $A_f = A\phi$ . This modification distinguishes constant and varying terms, where the varying term accounts for changes in the cross-sectional area available for the fluid. Equation 4 shows the modified continuity equation:

$$\frac{\partial(\rho_f \phi)}{\partial t} + \frac{\partial(\rho_f v A \phi)}{\partial z} = 0 \quad (4)$$

where  $A$  is the total cross-section of the extractor and  $\phi$  describes porosity along the extractor.

Assuming that the porosity and mass flow rate is constant in time, the temporal derivative becomes the mass flux  $F$ , and the spatial derivative can be integrated along  $z$  as

$$\int \frac{\partial(\rho_f v A \phi)}{\partial z} dz = F \rightarrow F = \rho_f v A \phi \quad (5)$$

To simplify the system dynamics, it is assumed that  $F$  is a control variable and affects the whole system instantaneously (due to  $\nabla \cdot u = 0$ ), which allows finding the velocity profile that satisfies mass continuity based on  $F$ ,  $\phi$  and  $\rho_f$ :

$$v = \frac{F}{\rho_f A \phi} \quad (6)$$

Similarly, superficial velocity may be introduced:

$$u = v \phi = \frac{F}{\rho_f A} \quad (7)$$

The fluid density  $\rho_f$  can be obtained from the Peng-Robinson equation of state if the temperature and thermodynamic pressure are known along  $z$ . Variation in fluid density may occur due to pressure or inlet temperature changes. In a non-isothermal case, in Equations 6 and 7  $\rho_f$  is considered the average fluid density along the extraction column.

#### 2.2.2. Mass balance for the fluid phase

Equation 8 describes the movement of the solute in the system, which is constrained to the axial direction due to the quasi-one-dimensional assumption. Given that the solute concentration in the solvent is negligible, the fluid phase is described as pseudo-homogeneous, with properties identical to those of the solvent itself. It is also assumed that the thermodynamic pressure remains constant throughout the device. The analysis further simplifies the flow dynamics by disregarding the boundary layer near the extractor's inner wall. This leads to a uniform velocity profile across any cross-section perpendicular to the axial direction. Thus, the mass balance equation includes convection, diffusion and kinetic terms representing the fluid phase behaviour:

$$\frac{\partial c_f}{\partial t} + \frac{1}{\phi} \frac{\partial(c_f u)}{\partial z} = \frac{1 - \phi}{\phi} r_e + \frac{1}{\phi} \frac{\partial}{\partial z} \left( D_e^M \frac{\partial c_f}{\partial z} \right) \quad (8)$$

where  $c_f$  represents the solute concentration in the fluid phase,  $r_e$  is the mass transfer kinetic term and  $D_e^M$  is the axial dispersion coefficient.

#### 2.2.3. Mass balance for the solid phase

As given by Equation 9, the solid phase is considered stationary, without convection and diffusion terms in the mass balance equation. Therefore, the only significant term in this equation is the kinetic term of Equation 10, which connects the solid and fluid phases. For simplicity, the extract is represented by a single pseudo-component:

$$\frac{\partial c_s}{\partial t} = \underbrace{-r_e}_{\text{Kinetics}} \quad (9)$$



### 2.2.4. Kinetic term

As the solvent flows through the fixed bed, CO<sub>2</sub> molecules diffuse into the pores, adsorb on the inner surface and form a film due to solvent-solid matrix interactions. The dissolved solute diffuses from the particle's core through the solid-fluid interface, the pore and the film into the bulk. Figure 2 shows the mass transfer mechanism, where the mean solute concentration in the solid phase is denoted as  $c_s$ , and the equilibrium concentrations at the solid-fluid interface are denoted as  $c_s^*$  and  $c_p^*$  for the solid and fluid phases, respectively. The concentration of the solutes in the fluid phase in the centre of the pore is denoted as  $c_p$ . As the solute diffuses through the pore, its concentration changes, reaching  $c_{pf}$  at the opening. Then, the solute diffuses through the film around the particle and reaches bulk concentration  $c_f$ . The two-film theory describes the solid-fluid interface inside the pore. The overall mass transfer coefficient can be determined from the relationship between the solute concentration in one phase and its equilibrium concentration.

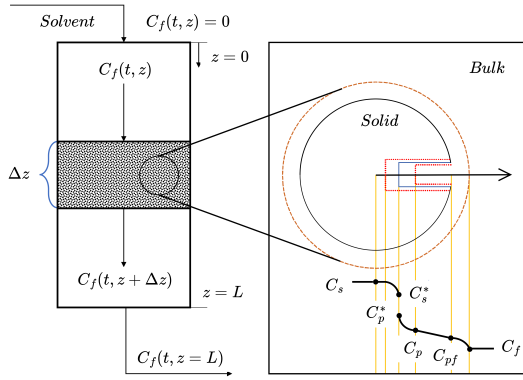


Figure 2: Mass transfer mechanism.

Bulley et al. [32] suggest a process where the driving force for extraction is given by the difference between the concentration of the solute in the bulk,  $c_f$ , and in the centre of the pore,  $c_p^*$ . The concentration  $c_p^*$  is in equilibrium with  $c_s$  according to the equilibrium relationship. The rate of extraction is thus  $r_e (c_f - c_p^*(c_s))$ . In contrast, Reverchon [24] proposes a driving force given by the difference between  $c_s$  and  $c_p^*$ . As given by Equation 10, the concentration  $c_p^*$  is determined by the equilibrium relationship with  $c_f$ :

$$r_e = \frac{D_i}{\mu l^2} (c_s - c_p^*) \quad (10)$$

where  $\mu$  is sphericity,  $l$  a characteristic dimension of particles that can be defined as  $l = r/3$ ,  $r$  is the mean particle radius,  $D_i$  corresponds to the overall diffusion coefficient and  $c_p^*$  is the concentration at the solid-fluid interface (which according to the internal resistance model is supposed to be at equilibrium with the fluid phase).

According to Bulley et al. [32], a linear equilibrium relationship (Equation 11) can be used to find the equilibrium concentration of the solute in the fluid phase  $c_f^*$  based on the concentration of the solute in the solid phase  $c_s$ :

$$c_f^* = k_p c_s \quad (11)$$

The volumetric partition coefficient  $k_p$  acts as an equilibrium constant between the solute concentration in one phase and the corresponding equilibrium concentration at the solid-fluid interphase. Spiro and Kandiah [33] proposed to define the mass partition coefficient  $k_m$  and the solid density  $\rho_s$  as

$$k_m = \frac{k_p \rho_s}{\rho_f} \quad (12)$$

According to Reverchon [24], the kinetic term becomes

$$r_e = \frac{D_i}{\mu l^2} \left( c_s - \frac{\rho_s c_f}{k_m \rho_f} \right) \quad (13)$$

### 2.2.5. Uneven solute's distribution in the solid phase

Following the idea of the Broken-and-Intact Cell (BIC) model (Sovova [34]), the internal diffusion coefficient  $D_i$  is considered to be a product of the reference value of  $D_i^R$  and the exponential decay function  $\gamma$ , as given by Equation 14:

$$D_i = D_i^R \gamma(c_s) = D_i^R \exp \left( -Y \left( 1 - \frac{c_s}{c_{s0}} \right) \right) \quad (14)$$

where  $Y$  describes the curvature of the decay function. Equation 15 describes the final form of the kinetic term:

$$r_e = \frac{D_i^R \gamma}{\mu l^2} \left( c_s - \frac{\rho_s c_f}{k_m \rho_f} \right) \quad (15)$$

The  $\gamma$  function limits the solute's availability in the solid phase. Similarly to the BIC model, the solute is assumed to be contained in the cells, some of which are open because the cell walls were broken by grinding, with the rest remaining intact. The diffusion of the solute from a particle's core takes more time than the diffusion of the solute close to the outer surface. The same idea can be represented by the decaying internal diffusion coefficient, where the decreasing term is a function of the solute concentration in the solid.

An alternative interpretation of the decay function  $\gamma$  involves considering the porous structure of the solid particles, where the pores are initially saturated with the solute. During extraction, the solute within these pores gradually dissolves into the surrounding fluid. Initially, the solute molecules near the pore openings dissolve and diffuse rapidly due to the short diffusion paths. As the extraction progresses, the dissolution front moves deeper into the pore structure, and solute from the inner regions of the pores begins to dissolve. The diffusion of solute molecules from the interior of the pores to the external fluid becomes progressively slower because the effective diffusion path length increases. This lengthening of the diffusion path enhances the mass transfer resistance, reducing the overall diffusion rate.

In an extreme case, this model could be compared with the Shrinking Core Model presented by Goto et al. [20], where the particle radius decreases as the solute content in the solid phase diminishes. In the SC model, the reduction in particle size leads to significant changes in both the diffusion path length and the surface area available for mass transfer. The diminishing particle size increases the diffusion path

within the remaining solid core and decreases the external surface area, both of which contribute to a slower extraction rate. By comparing this to the varying diffusion coefficient in our model, some conceptual similarities can be noticed.

### 2.2.6. Empirical correlations

The empirical correlations for  $D_i$  and  $\Upsilon$  were derived by Sliczniuk and Oinas [35] and validated for temperatures between 30 – 40 °C, pressures between 100 – 200 bar, and mass flow rates between  $3.33 - 6.67 \cdot 10^{-5}$  kg/s. Figures 3 and 4 show the results of multiple linear regression applied to solutions of parameter estimation and selected independent variables. The region marked with the white dashed line represents the confidence region, where the model has been tested. Both correlations should be equal or greater than zero, to avoid unphysical behaviour such as the reverse mass transfer. The multiple linear regression functions are combined with the rectifier function to ensure the non-negativity.

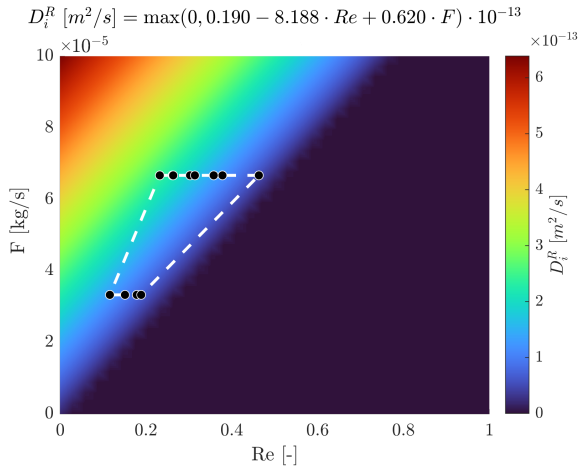


Figure 3: Multiple linear regression  $D_i^R = f(Re, F)$

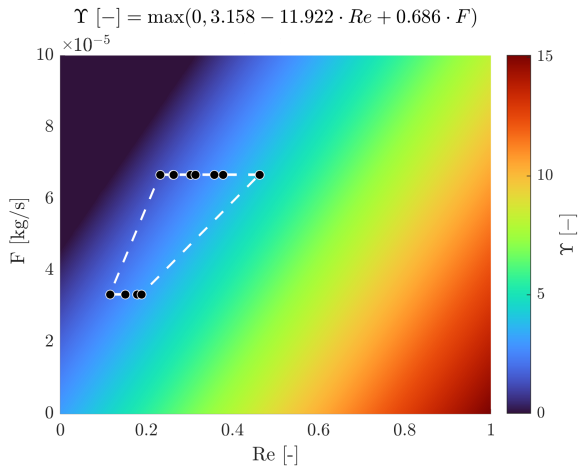


Figure 4: Multiple linear regression  $\Upsilon = f(Re, F)$

### 2.2.7. Heat balance

The heat balance equation describes the evolution of the enthalpy in the system and it is given by Equation 16

$$\frac{\partial (\rho_f h A_f)}{\partial t} = -\frac{\partial (\rho_f h A_f v)}{\partial z} + \frac{\partial (P A_f)}{\partial t} + \frac{\partial}{\partial z} \left( k \frac{\partial T}{\partial z} \right) \quad (16)$$

If the value of enthalpy  $h$  is known from the time evolution of the energy equation, and pressure  $P$  is known from measurement, then the temperature  $T$  can be reconstructed based on the departure function. The departure function is a mathematical function that characterizes the deviation of a thermodynamic property (enthalpy, entropy, and internal energy) of a real substance from that of an ideal gas at the same temperature and pressure. As presented by Gmehling et al. [36], for the Peng-Robinson equation of state, the enthalpy departure function is defined by Equation 17.

$$h - h^{id} = RT \left[ T_r(Z - 1) - 2.078(1 + \kappa) \sqrt{\alpha(T)} \ln \left( \frac{Z + (1 + \sqrt{2})B}{Z + (1 - \sqrt{2})B} \right) \right] \quad (17)$$

where  $\alpha$  is defined as  $(1 + \kappa(1 - \sqrt{T_r}))^2$ ,  $T_r$  is the reduced temperature,  $P_r$  is the reduced pressure,  $Z$  is the compressibility factor,  $\kappa$  is a quadratic function of the acentric factor and  $B$  is calculated as  $0.07780 \frac{P_r}{T_r}$ .

Equation 17 requires a reference state, which is assumed to be  $T_{ref} = 298.15$  K and  $P_{ref} = 1.01325$  bar.

A root-finder can be used to find a value of temperature, which minimizes the difference between the value of enthalpy coming from the heat balance and the departure functions. The root finding procedure is repeated at every time step to find a temperature profile along spatial direction  $z$ .

$$\min_T \left[ \underbrace{h(t, x)}_{\text{Heat balance}} - \underbrace{h(T, P, \rho_f(T, P))}_{\text{Departure function}} \right]^2 \quad (18)$$

### 2.2.8. Pressure term

As explained in Section 2.1, the pressure in the low-velocity region remains nearly constant due to the small pressure wave propagation occurring at the speed of sound. Under such conditions, the term  $\partial P / \partial t$  can be approximated by a forward difference equation, describing the pressure change over a small time step  $\Delta t$ . The pressure  $P$  in the system is treated as a state variable, while the incoming pressure at the new time-step  $P_{in}$  is treated as a control:

$$\frac{\partial P}{\partial t} \approx \frac{P_{in} - P}{\Delta t} \quad (19)$$

Such a simplified equation allows for instantaneous pressure. In a real system, the pressure dynamics would depend on the behaviour of the pump and the back-pressure regulator, which introduce additional inertia and resistance to pressure changes, leading to pressure gradual build-up.

### 2.2.9. Extraction yield

The process yield is calculated according to Equation 20 as presented by Sovova et al. [22]. The measurement

equation evaluates the solute's mass at the extraction unit outlet and sums it up. The integral form of the measurement (Equation 20) can be transformed into the differential form (Equation 21) and augmented with the process model.

$$y = \int_{t_0}^{t_f} \frac{F}{\rho_f} c_f \Big|_{z=L} dt \quad (20)$$

$$\frac{dy}{dt} = \frac{F}{\rho_f} c_f \Big|_{z=L} \quad (21)$$

### 2.2.10. Initial and boundary conditions

It is assumed that the solvent is free of solute at the beginning of the process  $c_{f0} = 0$ , that all the solid particles have the same initial solute content  $c_{s0}$ , and that the system is isothermal, hence the initial state is  $h_0$ . The fluid at the inlet is considered not to contain any solute. The initial and boundary conditions are defined as follows:

$$\begin{aligned} c_f(t=0, z) &= 0 & c_s(t=0, z) &= c_{s0} & h(t=0, z) &= h_0 \\ c_f(t, z=0) &= 0 & h(t, z=0) &= h_{in} & \frac{\partial c_f(t, z=L)}{\partial x} &= 0 \\ \frac{\partial h(t, z=L)}{\partial x} &= 0 & c_s(t, z=\{0, L\}) &= 0 & y(0) &= 0 & P(0) &= P_0 \end{aligned}$$

### 2.2.11. Discretization methods

$$\dot{x} = \frac{dx}{dt} = \begin{bmatrix} \frac{dc_{f,1}}{dt} \\ \vdots \\ \frac{dc_{f,N_z}}{dt} \\ \frac{dc_{s,1}}{dt} \\ \vdots \\ \frac{dc_{s,N_z}}{dt} \\ \frac{dh_1}{dt} \\ \vdots \\ \frac{dh_{N_z}}{dt} \\ \frac{dP}{dt} \\ \frac{dy}{dt} \end{bmatrix} = \begin{bmatrix} G_1(c_f, c_s, h; \Theta) \\ \vdots \\ G_{N_z}(c_f, c_s, h; \Theta) \\ G_{N_z+1}(c_f, c_s, h; \Theta) \\ \vdots \\ G_{2N_z}(c_f, c_s, h; \Theta) \\ G_{2N_z+1}(c_f, c_s, h; \Theta) \\ \vdots \\ G_{3N_z}(c_f, c_s, h; \Theta) \\ G_{3N_z+1}(c_f, c_s, h; \Theta) \\ \underbrace{G_{3N_z+2}(c_f, c_s, h; \Theta)}_{G(x; \Theta)} \end{bmatrix}$$

Figure 5: Discretized state-space

The method of lines is used to transform the process model equations into a set of ODEs denoted by  $G(x; \Theta)$ . For a derivative to be conservative, it must form a telescoping series. In other words, only the boundary terms should remain after adding all terms coming from the discretization over a grid, and the artificial interior points should be

cancelled out. Discretization is applied to the conservative form of the model to ensure mass conservation. The backward finite difference is used to approximate the first-order derivative, while the central difference scheme approximates the second-order derivative  $z$  direction. The length of the fixed bed is divided into  $N_z$ , i.e. equally distributed points in the  $z$  direction. The state-space model after discretization is denoted by  $x$  and defined as follows the Figure 5, where  $x \in \mathbb{R}^{N_x=3N_z+2}$  and  $\Theta \in \mathbb{R}^{N_\Theta=N_\theta+N_u}$ ,  $N_\theta$  is the number of parameters and  $N_u$  is the number of control variables.

## 2.3. Optimal design of experiment

### 2.3.1. Bayesian Estimation

After selecting a process model and estimating its parameters based on initial experiments, additional experiments may be planned to further refine the estimates of the model coefficients. An optimal experimental design enables parameters to be estimated without bias and with minimum variance. A model-based approach to experimental design allows for the consideration of system complexity and constraints, such as practical infeasibility due to safety concerns.

Building on the work of Walter and Pronzato [37] and Himmelblau [38], the Bayes' Theorem can be employed to define a general cost function:

$$\max p(\theta | Y, \Xi) = \frac{p(Y | \theta, \Xi) p(\theta)}{\int p(Y | \theta, \Xi) p(\theta) d\theta} \propto p(Y | \theta, \Xi) p(\theta) \quad (22)$$

The aim of experimental design is to maximize the posterior probability of estimating  $\theta$  ( $p(\theta | Y, \Xi)$ ) given the prior distribution of  $\theta$  ( $p(\theta)$ ) obtained from previous experiments, and the likelihood of obtaining observations  $Y$  ( $p(Y | \theta, \Xi)$ ) given  $\theta$  and experimental conditions  $\Xi$ . The new observations  $Y$ , under a set of experimental conditions  $\Xi$ , are assumed to be normally distributed around the model output  $y$ , with measurement error covariance  $\Sigma_Y$ . Similarly,  $\theta$  is assumed to be normally distributed around the true parameter values  $\hat{\theta}$ , with covariance matrix  $\Sigma_\theta$  estimated from previous experiments. These probabilities are:

$$p(Y | \theta, \Xi) = \frac{|\Sigma_Y|^{-1/2}}{(2\pi)^{n_Y/2}} \exp\left(-\frac{1}{2} (Y - y)^\top \Sigma_Y^{-1} (Y - y)\right) \quad (23)$$

$$p(\theta) = \frac{|\Sigma_\theta|^{-1/2}}{(2\pi)^{n_\theta/2}} \exp\left(-\frac{1}{2} (\theta - \hat{\theta})^\top \Sigma_\theta^{-1} (\theta - \hat{\theta})\right) \quad (24)$$

where  $n_Y$  is the number of observations and  $n_\theta$  is the number of parameters to be estimated. By substituting these expressions into the cost function:

$$\ln p(\theta | Y, \Xi) \propto -\frac{1}{2} \left[ (Y - y)^\top \Sigma_Y^{-1} (Y - y) + (\theta - \hat{\theta})^\top \Sigma_\theta^{-1} (\theta - \hat{\theta}) \right] \quad (25)$$

By linearizing the model output around  $\hat{\theta}$ , the model output becomes:  $y = y(\hat{\theta}) + J \Delta_\theta$ , where  $J = \frac{\partial y(\hat{\theta})}{\partial \theta}$  is the Jacobian matrix evaluated at  $\hat{\theta}$ , and  $\Delta_\theta = \theta - \hat{\theta}$ . To simplify the equation, the residual term  $\Delta_y = Y - y(\hat{\theta})$  is introduced. Substituting these into the expression for  $\ln p(\theta | Y, \Xi)$ :

$$\begin{aligned} \ln p(\theta | Y, \Xi) &\propto -\frac{1}{2} \left[ (\Delta_y - J \Delta_\theta)^\top \Sigma_Y^{-1} (\Delta_y - J \Delta_\theta) + \Delta_\theta^\top \Sigma_\theta^{-1} \Delta_\theta \right] \\ &= -\frac{1}{2} \left[ \Delta_y^\top \Sigma_Y^{-1} \Delta_y - 2 \Delta_y^\top \Sigma_Y^{-1} J \Delta_\theta + \Delta_\theta^\top (J^\top \Sigma_Y^{-1} J + \Sigma_\theta^{-1}) \Delta_\theta \right] \end{aligned}$$

This equation can be reformulated by expanding the quadratic terms:

$$\begin{aligned} \ln p(Y | \theta, \Xi) &\propto -\frac{1}{2} \left( \underbrace{r^T \Sigma_Y^{-1} r}_C - 2 \underbrace{J^T \Sigma_Y^{-1} \Delta_y \Delta_\theta}_B + \underbrace{\Delta_\theta^T (J^T \Sigma_Y^{-1} J + \Sigma_\theta^{-1}) \Delta_\theta}_A \right) \\ &= -\frac{1}{2} (\Delta_\theta^T \mathcal{A} \Delta_\theta - 2B^T \Delta_\theta + C) \end{aligned}$$

By completing the square, we introduce  $\theta^* = \hat{\theta} + \mathcal{A}^{-1}B$ , and the cost function becomes:

$$\ln p(\theta | Y, \Xi) \propto -\frac{1}{2} \left( (\theta - \theta^*)^T \mathcal{A} (\theta - \theta^*) + C - B^T \mathcal{A}^{-1} B \right) \quad (26)$$

It can be observed that the quadratic term represents the spread of the posterior multivariate distribution around the mean  $\theta^*$ . The constant term  $C - B^T \mathcal{A}^{-1} B$  is independent of  $\theta$  and does not affect the shape of the posterior distribution but is still important for normalization. This constant term is absorbed into the normalizing constant of the posterior distribution. It does not affect the estimation of  $\theta$  or the shape of the posterior distribution and thus can be neglected when focusing on parameter estimation or experimental design. Therefore, the posterior distribution of  $\theta$  given  $Y$  and  $\Xi$  is:

$$p(\theta | Y, \Xi) \propto \exp \left( -\frac{1}{2} (\theta - \theta^*)^T \mathcal{A} (\theta - \theta^*) \right) \quad (27)$$

This is the expression of a multivariate normal distribution with mean  $\theta^*$  and covariance matrix  $\mathcal{A}^{-1}$ :

$$p(\theta | Y, \Xi) = \mathcal{N}(\theta^*, \mathcal{A}^{-1}) \quad (28)$$

As the goal of optimal experimental design is to improve the precision of parameters, the main focus is on the matrix  $\mathcal{A}$ , which consists of two terms. The first corresponds to the information gained from new observations based on the model and measurement error ( $J^T \Sigma_Y^{-1} J$ ), while the second is the prior information ( $\Sigma_\theta^{-1}$ ).

### 2.3.2. Fisher Information

The Fisher Information  $\mathcal{F}$  measures the amount of information that an observable random variable carries about an unknown parameter of the distribution that models the random variable. It is related to the negative expected value of the second derivative of the log-likelihood function with respect to the parameter, providing a measure of how "sensitive" the likelihood is to changes in the parameter value.

$$\mathcal{F}(\theta, \Xi) = - \mathbb{E}_{Y|\theta, \Xi} \left[ \frac{\partial^2 \ln p(Y | \theta, \Xi)}{\partial \theta \partial \theta^T} \right] \quad (29)$$

Under regularity conditions, the Fisher Information can also be expressed as:

$$\mathcal{F}(\theta, \Xi) = \mathbb{E}_{Y|\theta, \Xi} \left[ \left( \frac{\partial \ln p(Y | \theta, \Xi)}{\partial \theta} \right) \left( \frac{\partial \ln p(Y | \theta, \Xi)}{\partial \theta} \right)^T \right] \quad (30)$$

By inserting the expression for  $p(Y | \theta, \Xi)$  and performing similar manipulations as in the previous section, the Fisher Information becomes:

$$\mathcal{F}(\theta, \Xi) = J^T \Sigma_Y^{-1} J \quad (31)$$

Since the likelihood is Gaussian and linearized, the second derivative of the log-likelihood with respect to  $\theta$

simplifies to  $J^T \Sigma_Y^{-1} J$ , and its negative expected value yields the same expression because the expectation of the Hessian is constant in this linear approximation.

The Cramér-Rao inequality provides that the covariance of any unbiased estimator  $\hat{\theta}$  satisfies:

$$\text{Cov}(\hat{\theta}) \geq \mathcal{F}^{-1}(\theta) \quad (32)$$

The precision with which a parameter  $\theta$  can be estimated is limited by the Fisher Information of the likelihood function. Based on the Cramér-Rao inequality, the Fisher Information matrix can be used to calculate the covariance matrices associated with maximum-likelihood estimates.

### 2.3.3. Optimal experimental design

The optimal design of experiments is a statistical concept that refers to the process of planning an experiment that allows parameters to be estimated without bias and with minimum variance. Optimal design ensures that the experiment can provide the most informative data possible. This often involves balancing the study of main effects and interactions between factors. Moreover, by efficiently planning experiments, optimal design aims to reduce the overall resources required, such as time, materials, and manpower.

The methodology for collecting data to estimate the parameters of a specific model is influenced by a series of qualitative decisions made throughout the experimental and modeling process, such as model structure, sensor locations, or equipment choices. Once these choices have been made, the experimenter still has some freedom to specify the quantitative experimental conditions (such as temperature, pressure, sampling times, etc.). Experiment design aims to determine experimental conditions adapted to the final purpose of the modeling.

Consider that each scalar observation in a study can be expressed as  $y(\xi_i)$ , where the  $n_\xi$ -dimensional vector  $\xi_i$  represents the specific experimental conditions (such as sampling time, operating conditions, etc.) under which the  $i$ -th observation is gathered. When collecting  $n_t$  such observations, the assembly of these  $\xi_i$  vectors forms the matrix  $\Xi = (\xi_1, \xi_2, \dots, \xi_{n_t})$ , which combines all the experimental conditions that need optimization. To align the design of the experiment with practical realities, it's important to take into account various constraints, such as the total duration of the experiments, the maximum temperature of the inlet stream, or the minimum interval between sampling events. The set of all possible combinations for  $\Xi$  that adhere to these constraints is denoted as  $\tilde{\Xi}$ .

The formulation of a cost function  $j$  allows for the framing of optimal experiment design as a problem of constrained optimization. In this context, the optimal experiment, denoted as  $\Xi^*$ , is:

$$\Xi^* = \arg \min_{\Xi \in \tilde{\Xi}} j(\Xi) \quad (33)$$

The cost function should describe the amount of information obtained from an experiment. For that purpose, it can be assumed that a function  $\kappa$  can be related to the covariance matrix  $\mathcal{A}^{-1}$  obtained at arbitrary operating conditions:

$$j(\Xi) = \kappa [\mathcal{A}^{-1}(\theta, \Xi)] \quad (34)$$



Recall that in the Bayesian estimation framework, the posterior covariance matrix of the parameter estimates is given by  $\Sigma = \mathcal{A}^{-1} = (J^T \Sigma_Y^{-1} J + \Sigma_\theta^{-1})^{-1}$ .  $J$  is the Jacobian matrix of the model outputs with respect to the parameters,  $\Sigma_Y$  is the covariance matrix of the measurement errors, and  $\Sigma_\theta$  is the prior covariance matrix of the parameters.

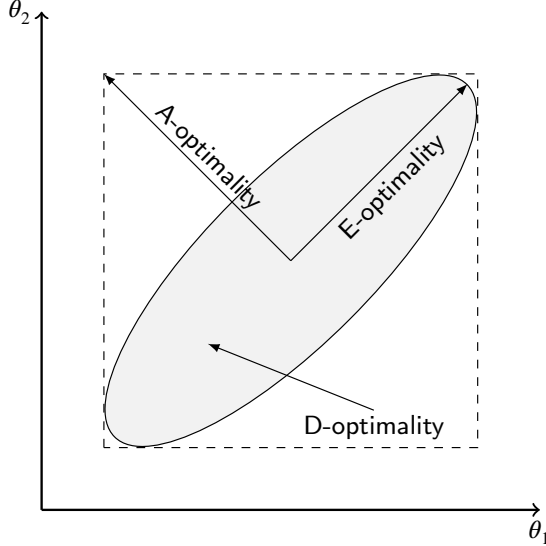


Figure 6: Graphical representation of score functions

A general class of design of experiments (DOE) optimality criteria is given by Equation 35. Some of the DOE criterion have graphical interpretation as shown in Figure 6.

$$\kappa_k(\mathcal{A}^{-1}(\theta)) = \begin{cases} \left[ \frac{1}{n_\theta} \text{trace}(\mathcal{Q} \mathcal{A}^{-1}(\theta, \Xi) \mathcal{Q}^T)^k \right]^{1/k} & \text{if } \det \mathcal{A}^{-1} \neq 0, \\ \infty & \text{if } \det \mathcal{A}^{-1} = 0 \end{cases} \quad (35)$$

where  $\mathcal{Q}$  is a weighting matrix. The special case  $k = 1$  corresponds to the L-optimality cost function:

$$j_L(\Xi) = \text{trace}(\mathcal{Q} \mathcal{A}^{-1}(\theta, \Xi) \mathcal{Q}^T) \quad (36)$$

Choosing  $\mathcal{Q} = \mathbf{I}_{n_\theta}$  corresponds to the A-optimality cost function. An A-optimal experiment minimizes the sum of the variances of the parameter estimates (i.e., the trace of the covariance matrix). When  $\mathcal{Q}$  is diagonal with  $[\mathcal{Q}]_{ii} = 1/\theta_i$ , this corresponds to weighting the parameters inversely by their magnitude, which is associated with relative precision.

Selecting  $\mathcal{Q}$  as a row vector results in C-optimality, which focuses on linear combinations of parameters. Setting  $\mathcal{Q} = \mathbf{I}_{n_\theta}$  and  $k = \infty$  leads to E-optimality, where the design maximizes the smallest eigenvalue of the covariance matrix  $\mathcal{A}^{-1}(\theta, \Xi)$ , thereby minimizing the length of the largest axis of the asymptotic confidence ellipsoids.

The most commonly used criterion is the D-optimality, which involves  $k = 0$  and  $\mathcal{Q} = \mathbf{I}_{n_\theta}$ , requiring the minimization of  $\det \mathcal{A}^{-1}(\theta, \Xi)$ , or equivalently, maximization of:

$$j_D(\Xi) = \det \mathcal{A}(\theta, \Xi) \quad (37)$$

Since  $\det \mathcal{A}(\theta, \Xi) = 1/\det \mathcal{A}^{-1}(\theta, \Xi)$ , maximizing  $\det \mathcal{A}$  is equivalent to minimizing  $\det \mathcal{A}^{-1}$ .

The D-optimality (D-OED) criterion originates from the geometric interpretation of the determinant. A two-dimensional matrix with real number entries can represent two linear maps: one mapping the standard basis vectors to the rows and the other to the columns. In both cases, the images of the basis vectors form a parallelogram that represents the image of the unit square under the mapping. The absolute value of the determinant is the area of this parallelogram, reflecting the scale factor by which the matrix transforms areas. The signed value of the determinant indicates the area of the parallelogram, which is negative when the angle from the first to the second defining vector is clockwise. In the multi-dimensional case, the matrix maps the n-cube to an n-dimensional parallelotope. The determinant provides the signed n-dimensional volume of this parallelotope, describing the volume scaling factor of the linear transformation produced by the matrix. Based on this geometrical interpretation, a D-optimal experiment minimizes the volume of the asymptotic confidence ellipsoids for the parameters.

### 2.3.4. Problem formulation

Details on the process model can be found in Sliczniuk and Oinas [35]. The model's empirical correlations are derived based on laboratory experiments conducted under various but constant operating conditions: 30–40 °C, 100–200 bar, and  $3.33 \cdot 10^{-5} - 6.67 \cdot 10^{-5}$  kg/s. This study employs the process model obtained previously to design a set of supplementary experiments with dynamically changing conditions to improve the precision of the correlation for  $D_i$ . The analyzed correlations consist of three independent variables: mass flow rate, pressure and inlet temperature.

In this work, the decision variables are the inlet temperature ( $T^{\text{in}}$ ) and mass flow rate ( $F$ ), while the pressure is assumed to remain constant during a batch. The optimal design of experiment problem is solved for multiple values of pressure: 100, 125, 150, 175, and 200 bar. The initial state is considered isothermal, so  $T^0(z) = T^{\text{in}}(t = 0)$ .

The decision variables are adjusted every 10 minutes and are kept constant within each interval (piecewise constant controls). These controls have lower and upper bounds that match the validated range of the process model detailed by Sliczniuk and Oinas [35]. The sampling time is assumed to be 5 minutes, and the total extraction time is 600 minutes. The standard deviation  $\sigma^2$  was estimated to be 0.03.

In a real system, the mass flow rate and inlet temperature cannot be changed instantaneously to any arbitrary value, as they depend on the dynamics of the pump and heat exchanger, respectively. To prevent bang-bang type of control, a penalty term is introduced. Inspired by control problems, such as the Linear Quadratic Regulator, a quadratic penalty term is added to the cost function. This penalty increases the cost function value when there are rapid changes in the decision variables. The matrix  $\mathcal{R}$  represents the control cost matrix, with its entries chosen so that the control costs are one order of magnitude lower than  $-\ln j_D$ . The problem formulation is given by Equation 38.

$$\Xi^* = \arg \min_{T^{\text{in}}(t), F(t)} \int_{t_0}^{t_f} \left[ -\ln j_D(\Xi, \dot{x}) + \frac{du(t)^T}{dt} \bar{R} \frac{du(t)}{dt} \right] dt,$$

subject to:  $\dot{x} = G(x, t, \theta; \Xi)$ ,  
 $t_0 = 0 \text{ min}, \quad t_f = 600 \text{ min},$   
 $T^0 = T^{\text{in}}(t = 0),$   
 $P(t) \in \{100, 125, 150, 175, 200\} \text{ bar},$   
 $31^\circ\text{C} \leq T^{\text{in}}(t) \leq 40^\circ\text{C},$   
 $3.33 \cdot 10^{-5} \leq F(t) \leq 6.67 \cdot 10^{-5},$   
 $\bar{R} = \begin{bmatrix} 0.1 & 0 \\ 0 & 0.01 \end{bmatrix},$   
 $\frac{du(t)}{dt} = \begin{bmatrix} \frac{dF(t)}{dt} \\ \frac{dT^{\text{in}}(t)}{dt} \end{bmatrix}.$

(38)

### 3. Results

To identify the global solution for Equations 38, the optimization problem is solved multiple times, each run starting from a random initial solution sampled from a uniform distribution. Figure 7 compares the initial and final cost function values across multiple optimization runs for all pressure cases. The solution with the lowest cost function value is considered the global solution for each case.

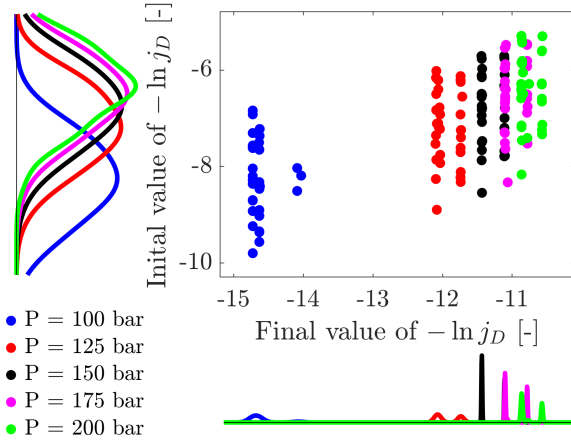
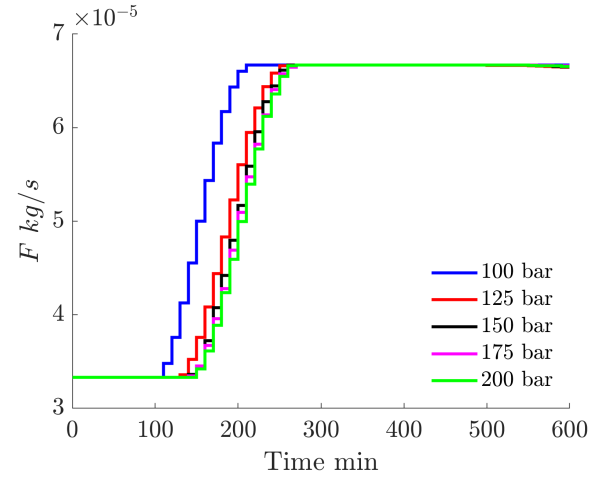


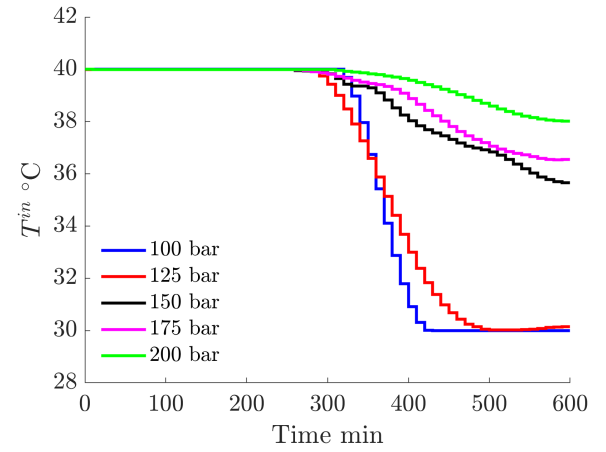
Figure 7: Initial vs final values of the cost function

By analyzing locations of the clusters in Figure 7, it can be concluded that experiments conducted near the critical point provide more information regarding the correlation than those conducted farther from it. For each pressure case, the solutions with the lowest value of the objective function are further analysed. The closer the pressure is to the critical point, the larger the deviations in the physical properties of  $\text{CO}_2$  caused by changes in the controls, leading to greater variation in the Reynolds number, and consequently to more informative experiments.

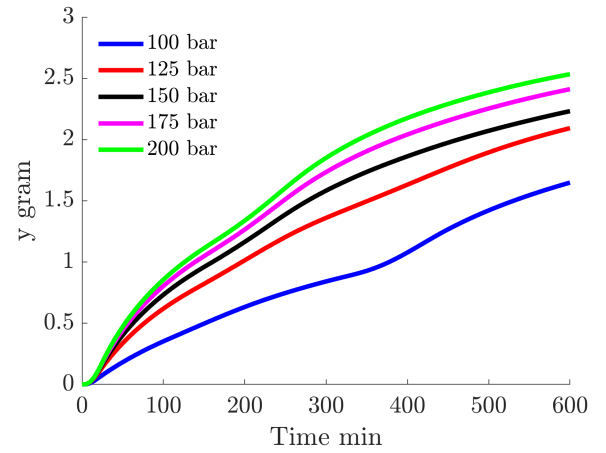
As presented in Figure 8a, all mass flow rate profiles initially stay at a minimum value, persisting for 100 to 150 minutes, depending on the pressure. Subsequently, a step-like increase in mass flow rate is observed, with the onset



(a) Optimal mass flow rate profiles



(b) Optimal inlet temperature profile



(c) Optimal yield profiles

Figure 8: Results of the optimization problem

occurring earlier at higher pressures. Between 250 and 300 min, the mass flow rate stabilizes at value of the upper bound.

Figure 8b shows the optimal profiles of the inlet temperature ( $T^{\text{in}}$ ) for various pressure cases in the supercritical  $\text{CO}_2$

extraction process. Initially, the  $T^{in}$  remains constant at approximately 40 °C for all pressures, indicating a stable starting condition for the system. The temperature decreases after about 300 min, but the exact time slightly varies depending on the pressure. This decline is rapid for lower pressures and gradual for higher pressures. The blue curve (100 bar) exhibits the sharpest temperature drop, while the green curve (200 bar) demonstrates a slower and more gradual decline. At lower pressures, the final temperature reaches the critical temperature and remains steady until the end of the batch. In contrary, the higher pressure cases result in a less significant temperature reduction. Moreover, the system does not reach steady operating conditions, as the inlet temperature profile does not flatten by the end of the process.

Figure 8c depicts the predicted yield curves. A closer examination of the yield and scatter plots reveals that the most informative experiments do not necessarily correspond to those with the highest yield. When the D-optimality criterion is applied, the aim is to maximize the determinant of the Fisher information matrix across the experimental design space. This approach identifies conditions that amplify variations in observed responses, particularly in regions with high sensitivity to parameter changes. As a result, the yield curve may display a "wavy" pattern, characterized by oscillations rather than a smooth, monotonic trend. These fluctuations arise from increased multiple critical points—local maxima, minima, or saddle points—on the response surface. By maximizing the sum of determinants of the Fisher information matrix, the experimental design prioritizes regions of high curvature, where the response changes sharply.

Alternatively, the D-optimality problem can be understood through the concept of Gaussian curvature. In this view, the experimental design shapes the parameter space of a model into a manifold with local geometry defined by the Fisher information matrix. The D-optimality condition maximizes the determinant of this matrix, which geometrically corresponds to maximizing the product of the principal curvatures of the manifold at a given point. This determinant is directly proportional to the Gaussian curvature, linking experimental design to the geometry of the parameter space. The determinant of the Fisher information matrix can be interpreted as a measure of the "volume element" on the parameter manifold, with higher values indicating regions of greater local curvature. By maximizing this determinant, the parameter manifold is locally as curved as possible, which explains the wavy behavior of the yield curves.

The results and observations discussed in this article are local and should be considered valid only for the model given by Sliczniuk and Oinas [35]. Although general conclusions about the curvature of the yield curve are independent of a process model, a completely different set of control profiles should be expected if the same technique is applied to a different model. Such strong dependence on a model is one of the most significant limitations of this work. Moreover, the model predicts the dataset in the region, which has not been validated during previous experiments. On one hand

this leaves a room for model validation, on the other hand the obtained set of data points might differs from the predictions.

## 4. Conclusions

This paper introduce the D-optimal experimental design (D-OED) as a model-based method for determining optimal experimental procedures in chemical engineering problems. D-OED optimizes an objective function, which can be geometrically interpreted as minimizing the volume of the uncertainty ellipsoid, thereby maximizing the precision of parameter estimates. Compared to the classical formulation of D-OED, this work introduces a penalty term to the cost function to prevent unrealistic rapid changes in operating conditions, ensuring practical feasibility in experimental implementation. The method is demonstrated through a case study on supercritical extraction, focusing on designing experiments to improve the precision of the correlation for the diffusivity coefficient  $D_i$ . While the original experiments were conducted under constant operating conditions, this study explores dynamically changing operating conditions, highlighting the potential of D-OED solutions for both parameter estimation and model validation.

The analysis was conducted for multiple pressure cases, and the optimal mass flow rate profiles were similar across all instances. The inlet temperature profiles show different patterns, but all of them start with high temperature and decrease in the second half of the batch. The resulting yield curves exhibit distinct wavy patterns, which can be explained through the relationship between the Hessian matrix and the Gaussian curvature of a multi-variable function. The determinant of the Fisher information matrix, central to the D-optimality criterion, is proportional to the Gaussian curvature of the parameter manifold. This curvature reflects the system's sensitivity to parameter changes and is maximized by the D-OED method. The observed wavy behavior of the yield curves is thus a manifestation of the high-curvature regions identified by the optimization, where the system's response to experimental conditions is most informative.

Further analysis of the yield curves and scatter plots reveals that the informativeness of experiments varies significantly across different operating conditions. This variation depends on the physical properties of CO<sub>2</sub>, which strongly change around the critical point. Consequently, it is concluded that operating conditions must be carefully selected to the specific regime of interest to maximize the information gained. This observation emphasizes the importance of aligning experimental strategies with the system's underlying physical properties and model structure.

## References

- [1] G. Sodeifian and S.A. Sajadian. Investigation of essential oil extraction and antioxidant activity of *echinophora platyloba* dc. using supercritical carbon dioxide. *The Journal of Supercritical Fluids*, 2017. ISSN 0896-8446. doi: 10.1016/j.supflu.2016.11.014.
- [2] E. Reverchon, G. Donsi, and L.S. Osseo. Modeling of supercritical fluid extraction from herbaceous matrices. *Industrial & Engineering Chemistry Research*, 1993. doi: 10.1021/ie00023a039.

- [3] H. Sovova. Rate of the vegetable oil extraction with supercritical CO<sub>2</sub>: modelling of extraction curves. *Chemical Engineering Science*, 49(3): 409–414, 1994. doi: 10.1016/0009-2509(94)87012-8.
- [4] E. Weidner. Impregnation via supercritical CO<sub>2</sub>—what we know and what we need to know. *The Journal of Supercritical Fluids*, 2018. ISSN 0896-8446. doi: 10.1016/j.supflu.2017.12.024.
- [5] N.D. Machado, J.E. Mosquera, R.E. Martini, María L. Goñi, and N.A. Gañán. Supercritical CO<sub>2</sub>-assisted impregnation/deposition of polymeric materials with pharmaceutical, nutraceutical, and biomedical applications: A review (2015–2021). *The Journal of Supercritical Fluids*, 191:105763, December 2022. ISSN 0896-8446. doi: 10.1016/j.supflu.2022.105763.
- [6] Arezu Ameri, Gholamhossein Sodeifian, and Seyed Ali Sajadian. Lansoprazole loading of polymers by supercritical carbon dioxide impregnation: Impacts of process parameters. *The Journal of Supercritical Fluids*, 164:104892, October 2020. ISSN 0896-8446. doi: 10.1016/j.supflu.2020.104892.
- [7] M. Fathi, G. Sodeifian, and S.A. Sajadian. Experimental study of ketoconazole impregnation into polyvinyl pyrrolidone and hydroxyl propyl methyl cellulose using supercritical carbon dioxide: Process optimization. *The Journal of Supercritical Fluids*, 188:105674, Sep 2022. ISSN 0896-8446. doi: 10.1016/j.supflu.2022.105674.
- [8] L. Padrela, M. A. Rodrigues, A. Duarte, Ana M.A. Dias, Mara E.M. Braga, and H. C. de Sousa. Supercritical carbon dioxide-based technologies for the production of drug nanoparticles/nanocrystals – a comprehensive review. *Advanced Drug Delivery Reviews*, 131:22–78, June 2018. ISSN 0169-409X. doi: 10.1016/j.addr.2018.07.010.
- [9] P. Franco and I. De Marco. Nanoparticles and nanocrystals by supercritical CO<sub>2</sub>-assisted techniques for pharmaceutical applications: A review. *Applied Sciences*, 11(4):1476, Feb 2021. ISSN 2076-3417. doi: 10.3390/app11041476.
- [10] G. Sodeifian, S.A. Sajadian, and R. Derakhsheshpour. CO<sub>2</sub> utilization as a supercritical solvent and supercritical antisolvent in production of sertraline hydrochloride nanoparticles. *Journal of CO<sub>2</sub> Utilization*, 2022. ISSN 2212-9820. doi: 10.1016/j.jcou.2021.101799.
- [11] G. Sodeifian and S.A. Sajadian. Solubility measurement and preparation of nanoparticles of an anticancer drug (letrozole) using rapid expansion of supercritical solutions with solid cosolvent (ress-sc). *The Journal of Supercritical Fluids*, 2018. ISSN 0896-8446. doi: 10.1016/j.supflu.2017.10.015.
- [12] N. S. Ardestani, G. Sodeifian, and S.A. Sajadian. Preparation of phthalocyanine green nano pigment using supercritical CO<sub>2</sub> gas anti-solvent (gas): experimental and modeling. *Heliyon*, 6(9):e04947, Sep 2020. ISSN 2405-8440. doi: 10.1016/j.heliyon.2020.e04947.
- [13] G. Sodeifian and S.A. Sajadian. Utilization of ultrasonic-assisted resolv (us-resolv) with polymeric stabilizers for production of amiodarone hydrochloride nanoparticles: Optimization of the process parameters. *Chemical Engineering Research and Design*, 2019. ISSN 0263-8762. doi: 10.1016/j.cherd.2018.12.020.
- [14] O. Singh, Z. Khanam, N. Misraand, and M.K. Srivastava. Chamomile (matricaria chamomilla l.): An overview. *Pharmacognosy Reviews*, 5 (9):82, 2011. ISSN 0973-7847. doi: 10.4103/0973-7847.79103.
- [15] J. Srivastava. Extraction, characterization, stability and biological activity of flavonoids isolated from chamomile flowers. *Molecular and Cellular Pharmacology*, 1(3):138–147, August 2009. ISSN 1938-1247. doi: 10.4255/mcparmacol.09.18.
- [16] A. Orav, A. Raal, and E. Arak. Content and composition of the essential oil of chamomilla recutita(l.) rauschert from some european countries. *Natural Product Research*, 24(1):48–55, Jan 2010. ISSN 1478-6427. doi: 10.1080/14786410802560690.
- [17] S. Milovanovic and A. Grzegorzcyk. A novel strategy for the separation of functional oils from chamomile seeds. *Food and Bioprocess Technology*, 2023. ISSN 1935-5149. doi: 10.1007/s11947-023-03038-9.
- [18] G. Sodeifian, S.A. Sajadian, and B. Honarvar. Mathematical modelling for extraction of oil from dracocephalum kotschy seeds in supercritical carbon dioxide. *Natural Product Research*, 2017. doi: 10.1080/14786419.2017.1361954.
- [19] G. Sodeifian, A.A. Sajadian, and N. Saadati Ardestani. Experimental optimization and mathematical modeling of the supercritical fluid extraction of essential oil from eryngium billardieri. *The Journal of Supercritical Fluids*, 2017. doi: 10.1016/j.supflu.2017.04.007.
- [20] M. Goto, B.C. Roy, and T. Hirose. Shrinking-core leaching model for supercritical-fluid extraction. *The Journal of Supercritical Fluids*, 9 (2):128–133, June 1996. doi: 10.1016/s0896-8446(96)90009-1.
- [21] H. Sovová, J. Kučera, and J. Jež. Rate of the vegetable oil extraction with supercritical CO<sub>2</sub>—ii. extraction of grape oil. *Chemical Engineering Science*, 49(3):415–420, 1994. ISSN 0009-2509. doi: 10.1016/0009-2509(94)87013-6.
- [22] H. Sovova, R. Komers, J. Kucuera, and J. Jezu. Supercritical carbon dioxide extraction of caraway essential oil. *Chemical Engineering Science*, 1994. doi: 10.1016/0009-2509(94)e0058-x.
- [23] K. D. Bartle, A. A. Clifford, S. B. Hawthorne, John J. Langenfeld, and R. Robinson. A model for dynamic extraction using a supercritical fluid. *The Journal of Supercritical Fluids*, 3(3):143–149, September 1990. ISSN 0896-8446. doi: 10.1016/0896-8446(90)90039-o.
- [24] E. Reverchon. Mathematical modeling of supercritical extraction of sage oil. *AIChE Journal*, 42(6):1765–1771, June 1996. ISSN 1547-5905. doi: 10.1002/aic.690420627.
- [25] R.A. Fisher. *The Design of Experiments*. Olivier & Boyd, 1935.
- [26] N.F. Ramandi, N.M. Najafi, F. Raofie, and E. Ghasemi. Central composite design for the optimization of supercritical carbon dioxide fluid extraction of fatty acids from borago officinalis l. flower. *Journal of Food Science*, 76(9), October 2011. ISSN 1750-3841. doi: 10.1111/j.1750-3841.2011.02394.x.
- [27] G. Caldera, Y. Figueroa, M. Vargas, and D.T. Santos. Optimization of supercritical fluid extraction of antioxidant compounds from venezuelan rosemary leaves. *International Journal of Food Engineering*, 8(4), October 2012. ISSN 1556-3758. doi: 10.1515/1556-3758.1953.
- [28] S.H. Chung, D.L. Ma, and R.D. Braatz. Optimal model-based experimental design in batch crystallization. *Chemometrics and Intelligent Laboratory Systems*, 50(1):83–90, January 2000. ISSN 0169-7439. doi: 10.1016/s0169-7439(99)00049-0.
- [29] B. Duarte, A. Atkinson, J. Granjo, and N. Oliveira. Calculating d-optimal designs for compartmental models with a michaelis–menten elimination rate. *Journal of Process Control*, 83:88–101, November 2019. ISSN 0959-1524. doi: 10.1016/j.jprocont.2019.09.001.
- [30] J. D. Jr Anderson. *Computational fluid dynamics: The basics with applications*. McGraw-Hill, 1995. ISBN 9780071132107.
- [31] J. D. Jr Anderson. *Fundamentals of Aerodynamics*. McGraw-Hill Education, 2023. ISBN 9781264151929.
- [32] N. R. Bulley, M. Fattori, A. Meisen, and L. Moyls. Supercritical fluid extraction of vegetable oil seeds. *Journal of the American Oil Chemists' Society*, 61(8):1362–1365, Aug 1984. doi: 10.1007/bf02542243.
- [33] M. Spiro and M. Kandiah. Extraction of ginger rhizome: partition constants and other equilibrium properties in organic solvents and in supercritical carbon dioxide. *International Journal of Food Science & Technology*, 25(5):566–575, June 2007. doi: 10.1111/j.1365-2621.1990.tb01116.x.
- [34] H. Sovova. Broken-and-intact cell model for supercritical fluid extraction: Its origin and limits. *The Journal of Supercritical Fluids*, 129:3–8, Nov 2017. doi: 10.1016/j.supflu.2017.02.014.
- [35] O. Slicznuk and P. Oinas. Mathematical modelling of essential oil supercritical carbon dioxide extraction from chamomile flowers. *The Canadian Journal of Chemical Engineering*, 2024. doi: 10.1002/cjce.25557.
- [36] J. Gmehling, M. Kleiber, B. Kolbe, and J. Rarey. *Chemical Thermodynamics for Process Simulation*. Wiley, Mar 2019. doi: 10.1002/9783527809479.
- [37] E. Walter and L. Pronzato. *Identification of parametric models from experimental data*. Communications and control engineering. Springer, London, 2010. ISBN 9781849969963.
- [38] David Mautner Himmelblau. *Process analysis by statistical methods*. Wiley, New York, 1970. ISBN 047139985X. [by] David M. Himmelblau., Includes bibliographical references.



**Nomenclature**

			$n_\theta$	Number of analysed parameters	-
			$n_Y$	Number of measurments	-
$\mathcal{A}$	Information matrix	-	$N_z$	Number of discretized points in z-direction	-
$B$	Weighted score vector	-	$P$	Pressure	bar
$C$	Weighted sum of squared deviations	-	$p$	Probaility disribution model	
$\mathcal{F}$	Fisher information	-	$P_r$	Reduced pressure	-
$\mathcal{R}$	Control cost matrix	-	$Q$	Weighting matrix	-
$A$	Total cross-section of the bed	$\text{m}^2$	$r$	Particle radius	m
$A_f$	Cross-section of the bed occupied by the fluid	$\text{m}^2$	$R_e$	Reynolds number	-
$B$	Pressure dependent parameter of P-R EoS	$\text{m}^2$	$r_e$	Mass transfer kinetic term	$\text{kg}/\text{m}^3/\text{s}$
$c_f$	Concentration of solute in the fluid phase	$\text{kg}/\text{m}^3$	$T$	Temperature	K
$c_f^*$	Concentration of solute at the solid-fluid interface	$\text{kg}/\text{m}^3$	$t$	Time	s
			$t_0$	Initial extraction time	s
$c_p$	Concentration of solute in the core of a pore	$\text{kg}/\text{m}^3$	$t_f$	Total extraction time	s
$c_s$	Concentration of solute in the solid phase	$\text{kg}/\text{m}^3$	$T_r$	Reduced temperature	-
$c_s^*$	Concentration of solute at the solid-fluid interface	$\text{kg}/\text{m}^3$	$T_{in}$	Inlet temperature	K
			$T_{out}$	Outlet temperature	K
$c_{f0}$	Initial concentration of solute in the fluid phase	$\text{kg}/\text{m}^3$	$u$	Superficial velocity	m/s
$c_{pf}$	Concentration of solute at the pore opening	$\text{kg}/\text{m}^3$	$v$	Linear velocity	m/s
$c_{s0}$	Initial concentration of solute in the solid phase	$\text{kg}/\text{m}^3$	$x$	State vector	
			$Y$	Yield measurement	g
$D_e^M$	Axial diffusion coefficient	$\text{m}^2/\text{s}$	$y$	Predicted extraction yield	g
$D_i$	Internal diffusion coefficient	$\text{m}^2/\text{s}$	$Z$	Compressibility factor	-
$D_i^R$	Reference value of internal diffusion coefficient	$\text{m}^2/\text{s}$	$z$	Spatial direction	m
<b>Greek symbols</b>					
$e$	Internal energy	J/kg	$\alpha$	Temperature-dependent function in the P-R EoS	-
$F$	Mass flow rate	kg/s	$\Delta_\theta$	Residial term of the parameters	-
$G$	Vector of discretized differential equations		$\Delta_y$	Residial term of the measurment error	g
$h$	Enthalpy	kJ/kg	$\epsilon$	Unobervable error	-
$J$	Jacobian	-	$\gamma$	Decaying function	-
$j$	Objective function	-	$\kappa$	Quadtratic function of the acentric factor	-
$k_m$	Mass partition coefficient	-	$\mu$	Sphericity coefficient	-
$k_p$	Volumetric partition coefficient	-	$\phi$	Bed porosity	-
$L$	Length of the fixed bed	m	$\pi$	Probability desnsity	-
$l$	Characteristic dimension of particles	m	$\rho_f$	Fluid density	$\text{kg}/\text{m}^3$

$\rho_s$	Bulk density of solid	kg/m <sup>3</sup>
$\Sigma$	Covariance matrix	-
$\sigma$	Standard deviation	-
$\Sigma_\theta$	Parameter uncertainty matrix	-
$\Sigma_Y$	Measurement covariance matrix	-
$\Theta$	Parameter space	-
$\theta$	vector of analysed parameters	-
$\Upsilon$	Decay coefficient	-
$\kappa$	An arbitrary function of $\mathcal{A}$	-
$\Xi$	Matrix of experimental conditions	-
$\xi$	Vector of experimental conditions	-

### Abbreviations

BIC	Broke-and-Intact Cell model
DoE	Design of Experiment
HBD	Hot Ball Diffusion
m-DoE	Model-based Design of Experiment
P-R EoS	Peng-Robinson Equation of State
SC	Shrinking Core
SFE	Supercritical Fluid Extraction